frontiers | Frontiers in Energy Research

TYPE Original Research
PUBLISHED 26 January 2023
DOI 10.3389/fenrg.2022.1080819

OPEN ACCESS

EDITED BY
Shichang Liu,
North China Electric Power University, China

REVIEWED BY
Mustafa Azeem,
Xi'an Jiaotong University, China
Di Yun,
Xi'an Jiaotong University, China

*CORRESPONDENCE
Lu Wu,
wulu1002@qq.com
Jing Zhang,
Jingzhang@nwpu.edu.cn

†These authors have contributed equally to this work

SPECIALTY SECTION
This article was submitted to Nuclear Energy, a section of the journal Frontiers in Energy Research

RECEIVED 26 October 2022
ACCEPTED 28 November 2022
PUBLISHED 26 January 2023

CITATION
Ma C, Zhao M, Xin T, Wu L, Pan R, Qin J and Zhang J (2023), Phase-field simulation of grain nucleation, growth, and Rayleigh distribution of U_3Si_2 nuclear fuel.
Front. Energy Res. 10:1080819.
doi: 10.3389/fenrg.2022.1080819

Phase-field simulation of grain nucleation, growth, and Rayleigh distribution of U_3Si_2 nuclear fuel

Cong Ma[1†], Min Zhao[1†], Tianyuan Xin[1], Lu Wu[1*], Rongjian Pan[1], Jiantao Qin[1] and Jing Zhang[2*]

[1]The First Sub-Institute, Nuclear Power Institute of China, Chengdu, China, [2]School of Material Science and Engineering, Northwestern Polytechnical University, Xi'an, China

U_3Si_2 is a potential accident-tolerant fuel (ATF) due to its high thermal conductivity and uranium density relative to UO_2. The grain size and distribution play an essential role in the service performance of U_3Si_2. However, the grain evolution is quite complicated and remains unclear, which limits further application of U_3Si_2 in the ATF assembly. In the present work, a phase-field model is employed to investigate the nucleation and growth of grains in U_3Si_2. Our results show that the number of grains rises rapidly at the nucleation stage until they occupy the whole system. After that, the grain radius and area continue to grow, and the grain number decays. The grain area increases in time according to the linear law, while the mean grain radius increases with time in a power law form with the scaling growth exponent z = 0.42, which is quite close to the theoretically predicted value. Finally, we performed statistical analysis and found that the grain size evolution of U_3Si_2 obeys Rayleigh distribution. Our simulation not only elucidates the nucleation and evolution of grains in U_3Si_2 during the thermal treatment process unambiguously but also provides a fundamental study on the investigation of grain growth, subdivision, and even amorphization in the irradiated condition, which is very important for U_3Si_2 used as ATF in the light water reactor.

KEYWORDS

U_3Si_2 fuel, phase-field simulation, grain nucleation and growth, exponential decaying, Rayleigh distribution

1 Introduction

Many novel nuclear fuels have been put forward to take the place of UO_2 since the Fukushima Daiichi accident. U_3Si_2 is extensively investigated among these fuels and is considered a promising next-generation ATF (Westinghouse Electric Company, 2015; Bischoff et al., 2016). Compared with the traditional UO_2 fuel, U_3Si_2 shows a series of unique advantages, such as higher thermal conductivity (λ equals ~ 7-8 W/(m·K) in UO_2 (Harding and Martin, 1989) and 15W/(m·K) in U_3Si_2 (White et al., 2015) at 573K, respectively), higher uranium density (11.31 g/cm^3 U in U_3Si_2 and 9.65 g/cm^3 U in UO_2) (White et al., 2015), and reinforced thermal conductivity at elevated temperature (White et al., 2015). All of these features can benefit superior safety in both regular operation and

the loss-of-coolant Accident (LOCA) (Terrani et al., 2014; Miao et al., 2017; Miao et al., 2018; Zhou and Zhou, 2018) and improve the power efficiency of the reactor.

The superior thermal conductivity and high uranium density promise U_3Si_2 an excellent accident-tolerant ability. In addition to this, the thermal properties and the mechanical performance are also determined by the fuels' microstructures. Manipulating grain and boundary areas through grain size control is essential for good performance. Generally, the fuels fail when they form a high burnup structure characterized by fine subgrain formation along grain boundaries. The grain boundaries are defect sinks that attract the gaseous fission products and vacancies, which cause bubbles nucleation and, consequently, severe stress concentration and swelling after. The gaseous atoms or small clusters dissolve the interior, cause limited lattice distortion, and are minor for swelling. The grain boundaries accommodate parts of fission gases that balance the interior and exterior of grains to maintain the performance stability. Grain coarsening or splitting into smaller subdivisions at the periphery at high temperatures and pressures will lead to out-of-balance, causing fuel failure.

U_3Si_2 consists of various grains with different crystallographic orientations. Many physical and chemical properties, such as corrosion resistance, thermal and electrical conductivity, mechanical properties (Davidge and Evans, 1969; Oguma, 1982; Kapoor et al., 2007), and fission gas release (Forsberg and Massih, 2001), depend on the mean grain size and distribution. However, due to the anisotropic crystallographic structure, grain evolution in U_3Si_2 is quite complicated. Up to now, even though there exist extensive investigations on U_3Si_2, the majority of these research studies focus on grain morphology. In contrast, grain growth, especially quantitative analysis of size distribution, is seldom investigated, which impedes the further understanding of grain subdivision and swelling behavior in U_3Si_2 under irradiation and restricts its extensive application in the field of ATF. Therefore, it is of great scientific and technological importance to investigate grain growth kinetics and perform a statistical analysis of grain evolution.

In recent years, with the rapid development of computer science and technology, numerical simulations have been gradually used to elucidate the mechanisms of grain growth spanning from the atomic to macroscopic scale (Atkinson HV, 1988). Computational studies are extremely useful since they permit isolation and analysis of the dominating factors of grain growth, contributing to microstructural evolution. Up to now, there have emerged various computational approaches to study microstructural evolution, such as the molecular dynamics (Azeem et al., 2019), Monte Carlo Potts model (Blikstein and Tschiptschin, 1999), surface evolver (Wakai et al., 2000), front tracking (Frost and Thopson, 1996), vertex dynamics (Weygand et al., 1998), cellular automata (Liu et al., 1997), and phase-field (Wen et al., 2006; Ansari et al., 2021) method. Among these methods, the phase-field approach has been extensively applied for grain growth modeling (Chen and Yang, 1994; Srezende et al., 1996; Fan and Chen, 1997; Kobayashi et al., 2000; Lobkovsky and Warren, 2001; III Krill and Chen, 2002) because it can deal with a large system involving thousands of grains, track individual grain boundaries, and apply specific constitutive relations to their motion. Currently, there are two main phase-field models for grain growth simulation. The earliest and most widely used model was developed by Chen and Yang, in which the grains of different crystallographic orientations are represented by a set of nonconserved order parameter fields (Chen and Yang, 1994). This model can be used in 2D (Fan and Chen, 1997) and 3D (III Krill and Chen, 2002) phase-field modeling simulations of grain growth. Srezende et al. proposed another class of multiphase-field model (Srezende et al., 1996) with a constraint on the order parameters, such that the sum of all order parameters at a given point yields unity, and the order parameters can represent the volume fraction of grains of different orientations. According to experimental data and molecular dynamics (M.D.) simulation results (Beeler et al., 2019), Cheniour et al. (2020) set up a phase-field model and investigated how grain size changes with time under ideal circumstances by giving a quantitative relationship. Nevertheless, how the microstructure evolves and whether an underlying mechanism dominates this process remain unknown.

In this work, we systematically investigated grain nucleation and growth in U_3Si_2 during thermal treatment through phase-field simulation. Microstructure evolution and grain size distribution within different thermal treatment stages are well examined. Our results show that the average grain size varies with time in a power law form, and grain size evolution in U_3Si_2 obeys Rayleigh distribution. Our work is organized as follows. Section 2 presents the phase-field formalism for grain growth and microstructure evolution modeling. Section 3.1 shows our simulated microstructure evolution of U_3Si_2 with thermal treatment time, while Section 3.2 and Section 3.3 exhibit the statistical method and result for corresponding grain size and distribution, respectively. Finally, in Section 4, we provide the main conclusions.

2 Phase-field model of grain nucleation and growth

Phase field is a mesoscale method that adopts the Ginzburg–Landau free energy constructed with one or multiple order parameters to depict the symmetry breaking of the system. The equation of motion for the phase-field methodology generally adopts the Cahn–Hilliard equation for conserved fields and the Allen–Cahn equation for nonconserved fields. It accommodates the macro contribution from ingredients and the environment, as well as the micro information on the surface and local stress heterogeneity. The phase-field method for grain growth of various metallics and ceramics has provided

valuable knowledge (Chen and Yang, 1994; Chen, 2002; Rest and Hofman, 2004; Millett et al., 2008; Ahmed et al., 2014; Tonks et al., 2014; Liang et al., 2016; Mei et al., 2016; Li et al., 2017; Cheniour et al., 2020), inspiring the understanding of U_3Si_2.

This work concerns the grain nucleation and growth of U_3Si_2, and nonconserved order parameters and the Allen–Cahn-type dynamic equation are adopted. The grain boundary energy and mobility of grains with different orientations are well formulated. The free energy is a function of the distribution of the order parameters. The grains were characterized by a set of order parameters $\{\eta_i\}_{i=1}^{n}$ for a microstructure consisting of n grains. A grain i is characterized by $\eta_i = 1$ and $\eta_{i \neq j} = 0$. The grain boundary is characterized by a smooth order parameter ranging from 0 to 1. The effective total free energy F describing the grain microstructure has the following form:

$$F = \int dr \left\{ F_0 \left[\sum_{i=1}^{M} \left(\frac{\eta_i^4}{4} - \frac{\eta_i^2}{2} \right) + \sum_{i=1}^{M} \sum_{i \neq j}^{M} \gamma_{ij} \eta_i^2 \eta_j^2 \right] + \frac{\mathrm{K}}{2} \sum_{i=1}^{M} |\nabla \eta_i|^2 \right\}, \tag{1}$$

where F_0 is the free-energy barrier coefficient,∇ is the Nabla operator, κ is the gradient energy coefficient, and γ_{ij} is the interface energy coefficient.

Using the free-energy functional, we can compute the specific grain boundary energy of the system of two grains η_i and η_j (with a flat interface $x = 0$ in a one-dimensional case) (Aagesen et al., 2020), which is given by the integral

$$\gamma = \int_{-\infty}^{+\infty} \left[F_0 f\left(\eta_i, \eta_j\right) + \frac{\kappa}{2} \left(\left(\nabla_x \eta_i\right)^2 + \left(\nabla_x \eta_j\right)^2 \right) \right] dx, \tag{2}$$

where x is the coordinate perpendicular to the grain boundary. A topographical view of the free-energy density (the term in square brackets in Eq. 1) is shown in Moelans et al. (2008a).

According to the principles of variational calculus, the functions $\eta_i(x)$ and $\eta_j(x)$ that extremize functional Eq. 1 satisfy the following equations:

$$\begin{aligned} F_0 \frac{\partial f}{\partial \eta_i} - \kappa \nabla_{xx}^2 \eta_i = 0, \\ F_0 \frac{\partial f}{\partial \eta_j} - \kappa \nabla_{xx}^2 \eta_j = 0. \end{aligned} \tag{3}$$

Or, equivalently, the integrated equation

$$F_0 f\left(\eta_i, \eta_j\right) - \frac{\kappa}{2} \left(\left(\nabla_x \eta_i\right)^2 + \left(\nabla_x \eta_j\right)^2 \right) = 0, \tag{4}$$

where boundary conditions are taken into account, the rearrangement of this equation gives

$$\nabla_x \eta_i = \sqrt{\frac{2F_0 f\left(\eta_i, \eta_j\right)}{\kappa \left(1 + \left[\partial \eta_i / \partial \eta_j\right]^2\right)}}, \nabla_x \eta_j = \sqrt{\frac{2F_0 f\left(\eta_i, \eta_j\right)}{\kappa \left(1 + \left[\partial \eta_j / \partial \eta_i\right]^2\right)}}. \tag{5}$$

A combination of these two equations in Eq. 4 gives

$$\begin{aligned} \gamma &= 2F_0 \int_{-\infty}^{+\infty} f\left(\eta_i, \eta_j\right) dx \\ &= \sqrt{2F_0 \kappa} \int_0^1 \sqrt{f\left(\eta_i, \eta_j\left(\eta_i\right)\right)} \sqrt{1 + \left[\frac{\partial \eta_j}{\partial \eta_i}\right]^2} d\eta_i. \end{aligned} \tag{6}$$

The model energetic parameter F_0 and interfacial energies γ_{ij} between grains and the gradient energy coefficient that penalizes non-zero gradients of the variables across the grain boundary can be expressed through the mean grain boundary energy $\bar{\gamma}$ and grain boundary interaction length l_{int} and grain boundary mobility $\bar{M}$ as follows (Moelans et al., 2008a; Moelans et al., 2008b):

$$\gamma = g\left(\gamma_{ij}\right) \sqrt{\kappa F_0}, \kappa = \frac{3}{4} \gamma l_{\mathrm{int}}, F_0 = \frac{6\gamma}{l_{\mathrm{int}}}, l_{\mathrm{int}} = \sqrt{8\kappa / F_0}. \tag{7}$$

As usual, for the special case $\gamma_{ij} = \frac{3}{2}$, it results to $g(\gamma_{ij} = 3/2) = \sqrt{2}/3$ (Aagesen et al., 2020).

The interface profile can be obtained by considering a symmetrical case, where $\eta_j = 1 - \eta_i$. In such a case, one gets

$$\nabla_x \eta_j = -\nabla_x \eta_i, \quad \nabla_{xx}^2 \eta_j = -\nabla_{xx}^2 \eta_i, \quad \frac{\partial \eta_j}{\partial \eta_i} = -1, \quad \frac{\partial \nabla_x \eta_j}{\partial \nabla_x \eta_i} = -1. \tag{8}$$

When applying $\gamma_{ij} = \frac{3}{2}$, one can get profiles from equations:

$$\begin{aligned} \nabla_{xx}^2 \eta_j &= \frac{F_0}{\kappa} \left(2\eta_i \left(2\eta_i^2 - 3\eta_i + 2\right)\right), \\ \nabla_{xx}^2 \eta_i &= \frac{F_0}{\kappa} \left(2\eta_j \left(2\eta_j^2 - 3\eta_j + 2\right)\right), \end{aligned} \tag{9}$$

$$\nabla_x \eta_i = -\sqrt{\frac{2F_0}{\kappa}} \eta_i \left(1 - \eta_i\right), \quad \nabla_x \eta_j = -\sqrt{\frac{2F_0}{\kappa}} \eta_j \left(1 - \eta_j\right). \tag{10}$$

The Allen–Cahn dynamical equation has the following form:

$$\partial_t \eta_i = -L_{\eta_i} \frac{\delta F}{\delta \eta_i} + \xi_v, \tag{11}$$

where $L_{\eta_i} = \frac{\bar{M}\gamma}{\kappa}$ and $L_{\eta i}$ is mobility. In order to embody the thermal fluctuations, we added noise terms ξ_v determined by the fluctuation–dissipation theorem to the governing Eq. 11. Substituting the free energy of Eq. 1 into Eq. 11, the numerical solution for Eq. 11 will give the temporal and spatial evolution of grains.

To compute appropriate values of both F_0 and κ, one can put $l_{\mathrm{int}} = \omega \delta_G$, where δ_G is the width of the grain boundary and ω is the constant defining diffusion grain boundary. In the computation procedure, the mesh size Δl is chosen in as $\Delta l = 3.33\delta_G$, by taking values for F_0 and κ from Rest and Hofman (2004). For all problem quantities of the order unity, the governing equations were non-dimensionalized using length, time, and energy scales $E^* = 63 \times 10^9 J/m^3$. Therefore, we can describe the parameterization of the order parameter mobility L_{η_i}. Using that approach, we set $\bar{L} = 1$, which leads to a dimensional value $L_{\eta_i} = \frac{\bar{L}}{E^* t^*} = 1.59 \times 10^{-10} m^3/(Js)$ (Aagesen et al., 2020). The physical parameters used for phase-field simulations are summarized in Table 1.

TABLE 1 Parameters used for phase-field simulations.

Parameter	Value
F_0	$6.84 \times 10^8 J/m^3$
κ	$1.92 \times 10^{-8} J/m$
ω	10
Δl	$10.7nm$
l_{int}	$20.7nm$
γ_{ij}	3/2
L_{η_i}	$1.59 \times 10^{-10} m^3/(Js)$
T	$600K$
N	256, 512

3 Simulation results and mathematical statistical analysis

3.1 Microstructure evolution

The simulations were performed at a typical operating temperature of 600 K with the characteristic length $L = N\Delta l$ on a mesh grid of 256 and 512 with $\Delta l = 10.7nm$. The implicit Fourier transformation method is employed to solve the Allen–Cahn equation. The iteration step t represents the time advances, and the unit of time is minute. A typical scenario of the grain nucleation and growth within a 256-mesh grid is shown in Figure 1. Several nuclei form at the beginning and grow up subsequently. It is well seen that grain nucleation and growth proceed simultaneously; the previously formed grains grow in size and interconnect with other growing grains. This process occurs until all grains are connected through grain boundaries. The value of the order parameter inside each grain is $\eta_i = 1$; at grain boundaries, it takes values less than 0.5, and it corresponds well to the prediction by the model. Moreover, we find that grains with several sides $n \neq 6$ are unstable, and they can grow or decrease the size depending on the neighbor grains' configuration.

3.2 Statistical analysis of the average grain size

It can be found that the grain boundary (G.B.) energy and mobility are the two main parameters required to be determined for grain growth in U_3Si_2, based on the analysis and research of Cheniour et al. (2020). During normal grain growth, the applied pressure on a grain boundary is given by

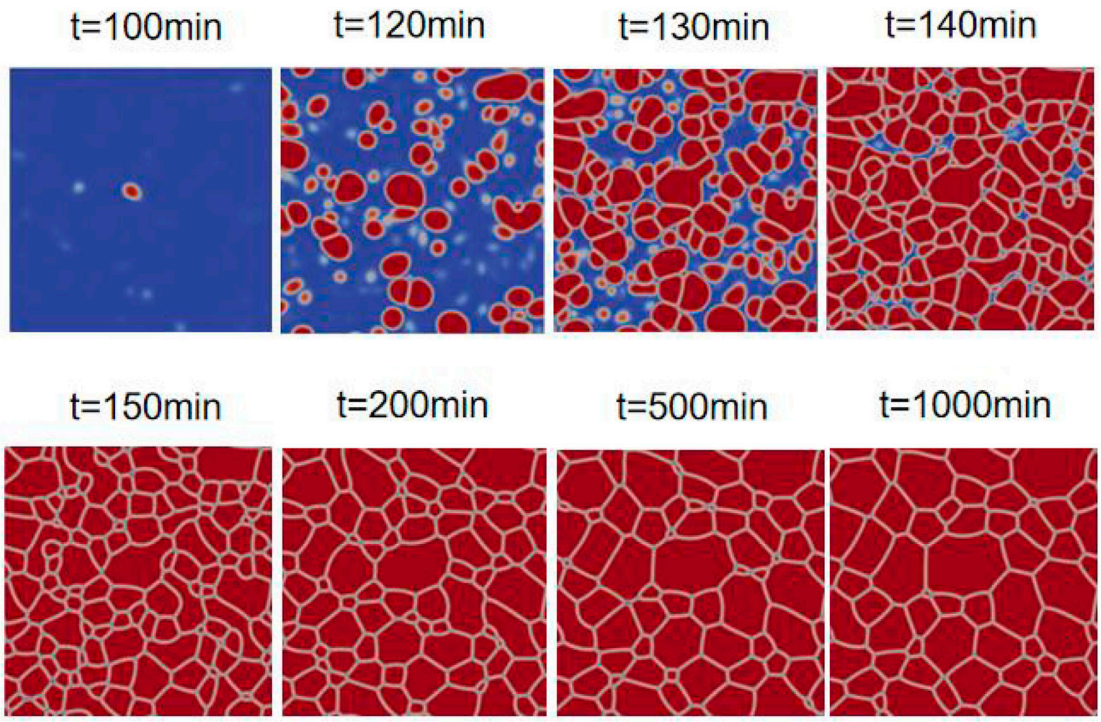

FIGURE 1
Typical scenario of the system evolution with N = 256, L = 2.739 μm, and T = 600 K, at various timesteps t.

$$P_a = \frac{\gamma}{R}, \tag{12}$$

where γ is the grain boundary energy and R is the radius of grain curvature. The grain boundary velocity is

$$v \equiv \frac{dR}{dt} = M(P_a - P_r) \geq 0, \tag{13}$$

where the constant M relates to the grain mobility andP_r is the resistive pressure. Sources of this resistive pressure include voids, pores, and precipitates that cannot diffuse with the boundary. As a result of grain growth, when the driving pressure P_a falls to the value P_r, there is no net pressure, and grain growth ceases at a limiting value. The term P_r is similar to the Zener pinning (Li et al., 2021) term, which accounts for a limiting grain size in two-phase materials.

The average grain size is defined as

$$D \equiv \alpha^{1/2}\overline{R}, \tag{14}$$

where grain topology is included into the geometric constant α. Therefore, dynamics of the grain size obey the following equation:

$$\partial_t D = \alpha\bar{M}\left(\frac{\bar{\gamma}}{D} - \alpha^{-1/2}P_r\right). \tag{15}$$

Here, $\bar{M}$ and $\bar{\gamma}$ are the averaged grain boundary mobility and energy, respectively. When taking into account the simplest case of no resistive pressure, one finds the solution in the form

$$D^2 - D_0^2 = Kt, \quad K \equiv 2\alpha\bar{M}\bar{\gamma}. \tag{16}$$

Temperature dependence of the grain boundary energy for U_3Si_2 by MD simulations (Beeler et al., 2019) was found:

$$\bar{\gamma}(T) = H(T) - TS(T), \tag{17}$$

$$H(T) = 1.21 \times 10^{-7}T^2 - 3.46 \times 10^{-5}T + 0.85 J/m^2, \tag{18}$$

$$S(T) = 4.58 \times 10^{-7}T - 1.72 \times 10^{-4} J/m^2K. \tag{19}$$

The rate constant and grain mobility dependencies on temperature were measured by experimental data (Cheniour et al., 2020):

$$K = 8.77 \times 10^{-18} \exp(-0.33eV/k_BT) m^2/s, \tag{20}$$

$$\bar{M} = 6.30 \times 10^{-18} \exp(-0.33eV/k_BT) m^4/Js. \tag{21}$$

By comparing Eqs 16, 17, 20, 21, we can obtain: $\alpha = 0.96$

Data analysis allows one to obtain the grain area, mean grain size, and amount of grains computed directly from the simulation procedure. The corresponding results are shown in Figure 2 for systems of the linear size L = 2.739 μm and L = 5.478 μm. From Figure 2A, it is seen that the grain area increases in time, according to the linear time law. Our simulated grain size is ~180 nm, which is two orders of magnitude smaller than the experimental values (between 16 and 18 μm from an initial irradiation experiment). It is to be noted that many factors, such as irradiation and heat treatment time, can influence the grain size; our simulation still can act as a reference for grain morphology investigation after heat treatment in the experiment. From Figure 2B one finds that the mean grain radius increases in time in a power law form with a scaling growth exponent of 0.42, which is

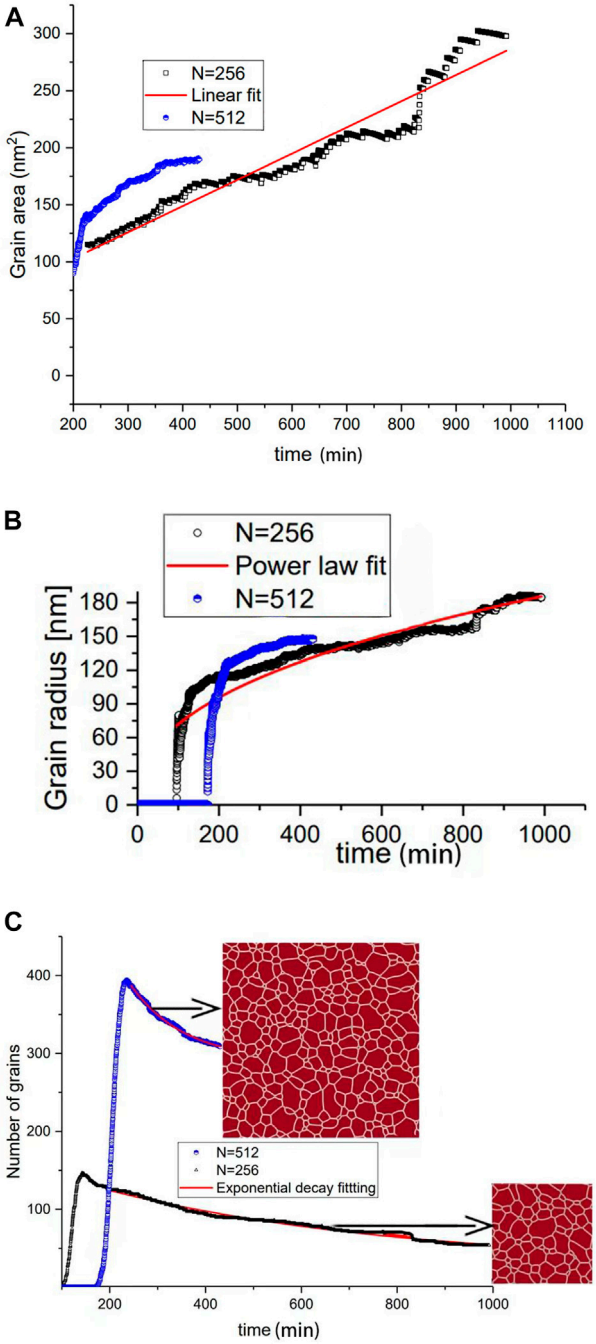

FIGURE 2
(A) Grain area dynamics,**(B)** grain radius dynamics, and **(C)** number of grains at N = 256 and L = 2.739 μm, and N = 512 and L = 5.478 μm.

quite close to the theoretically predicted value, 1/2 (Cheniour et al., 2020). It is important that this grain size variation is observed at a late stage when grain grows following the Ostwald ripening scenario in which large grains grow by consuming the small ones. In Figure 2C, we plot the time dependencies of the grain amount. It follows that the grain number increases rapidly at grain nucleation stages until grains occupy the whole system volume. One can clearly observe the scaling dynamics of the grain radius and area at the later stage when the number of grains decays. Usage of the fitting procedure allows one to find that this kind of decrease can be described well by the exponential decaying function; the exponential decaying function in red in Figure 2C coincides with the simulation results. One must point out that obtained results concerning the scaling behavior of described values are independent of the system size. The size of the system affects only the grain size and their amount due to the influence of periodic boundary conditions and a lack of grains with different morphology, as observed in systems with large sizes.

3.3 Statistical analysis of grain distribution

In general, Eq. 13 is written for the mean radius of grains. In further consideration, we put resistive pressure equals to zero and assume that some grains can decrease in size due to a change in the number of edges. During the system's evolution, the grains with edges of fewer than six disappear. This process is reoccurrence through a relaxation process with time τ_R. In such a case, we introduce a grain size distribution function $\Psi(R)$ that gives the grain density with radius R; then, $\Psi(R)dR$ is the total grains in a grain radius ranging between R and $R + dR$, and dR is a small increment of the grain radius. The growth and relaxation of grains are described as

$$\begin{aligned}\left[\frac{d\Psi}{dt}\right]_g dR &= -\frac{d}{dR}\left[\Psi(R)\frac{dR}{dt}\right]dR\\ \left[\frac{d\Psi}{dt}\right]_r &= -\Psi(R)/\tau_R.\end{aligned} \tag{22}$$

The total net change of the concentration of grains is

$$\left[\frac{d\Psi}{dt}\right]_{tot} = \left[\frac{d\Psi}{dt}\right]_g + \left[\frac{d\Psi}{dt}\right]_r. \tag{23}$$

An equilibrium grain population is defined in a stationary case resulting in the following equation:

$$\frac{d\Psi(R)}{dR_0}v(R) + \Psi(R)\frac{dv(R)}{dR} + \Psi(R)/\tau_R = 0. \tag{24}$$

A solution of Eq. 22 for the distribution function can be found in quadratures:

$$\begin{aligned}\Psi(R) &= \frac{C_0}{v(R)}\exp\left(-\frac{1}{\tau_R}\int_{R_0}^{R}\frac{dR'}{v(R')}\right),\\ C_0^{-1} &= \int_{R_0}^{\infty}\Psi(R)dR,\end{aligned} \tag{25}$$

where $v(R)$ is defined in Eq. 13, and C_0 is the integration constant giving the total number of grains.

Based on the substituting growth speed Eq. 16 into Eq. 25 and assuming $P_r \to 0$, one gets the Rayleigh distribution function:

$$\Psi(R) = \frac{C_0 R}{R_0\bar{M}\bar{\gamma}}\exp\left(-\frac{(R^2 - R_0^2)}{2\tau_R\bar{M}\bar{\gamma}}\right). \tag{26}$$

This distribution can be used in a fitting procedure to describe numerically obtained results and experimental observations.

In addition, in a nonstationary case, we exploit the Fourier method:

$$\begin{aligned}\Psi(R,t) &= \psi(t)\bar{\omega}\left(\frac{R(t)}{a(t)}\right),\\ y &= \frac{R(t)}{a(t)},\end{aligned} \tag{27}$$

where y is the grain radius scaled in a(t); $\psi(t)$ andϖ(y) are unknown functions. The time derivative of the grain radius is scaled as

$$dR/dt = \theta(t)\sigma(y), \tag{28}$$

where the corresponding time dependence defined by $\theta(t)$ should coincide with $\dot{a}(t)$, following the definition of the grain size derivative:$\theta(t) \equiv \dot{a}(t)$.

Through substituting time derivatives and spatial derivatives as $d\Psi/dt = \varpi(y)\dot{\psi}$, $dR/dt = \sigma(y)\dot{a}$, and $d/dR = d/ady$, one can separate parts describing time dependencies and size dependencies in the following form:

$$\frac{a(t)}{\dot{a}(t)}\left(\frac{\dot{\psi}(t)}{\psi(t)} + \tau_R^{-1}\right) = \frac{1}{\varpi(y)}\frac{d}{dy}\sigma(y)\varpi(y). \tag{29}$$

Next, we set both sides of Eq. 29 to the same constant $-C$ with $C > 0$; one gets two separate equations for time dependence and grain size dependence:

$$\frac{\dot{\psi}(t)}{\psi(t)} = -C\frac{\dot{a}(t)}{a(t)} - \tau_R^{-1}, \tag{30}$$

$$-C\varpi(y) = \frac{d}{dy}\sigma(y)\varpi(y). \tag{31}$$

Furthermore, we can get the following two equations of the form:

$$\psi(t) = \psi_0[a(t)]^{-C}\exp(-t/\tau_R), \tag{32}$$

$$\varpi(y) = \frac{\varpi_0}{\sigma(y)}\exp\left(-C\int_0^y\frac{dy'}{\sigma(y')}\right), \tag{33}$$

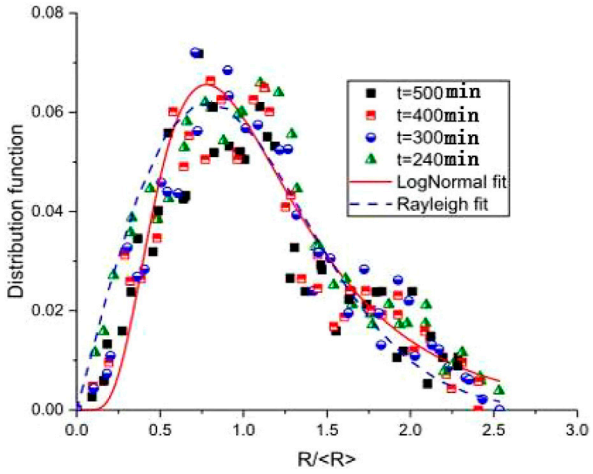

FIGURE 3
Grain size distribution function at N = 512 and L = 5.478 μm.

where ψ_0 and ϖ_0 are integration constants. Based on the aforementioned conclusions, we can further obtain the following formulas:

$$N(t) = N_0[a(t)]^{1-C}\exp(-t/\tau_R), \quad N_0 = \psi_0\int_0^\infty \varpi(y)dy, \tag{34}$$

$$R(t) = R_0 a(t), \quad R_0 = \frac{\int_0^\infty y\varpi(y)dy}{\int_0^\infty \varpi(y)dy}, \; a(t) \propto t^z. \tag{35}$$

Figure 3 shows our simulated grain size distribution along with grain area evolution at different times. It follows that all data are lying in statistically the same trend. Our result manifests a universal grain size distribution function as was predicted by theoretical studies (Vaz and Fortes, 1988). More importantly, the fitting procedure allows one to choose a more accurate distribution function for describing objects like voids, bubbles, and grains. In our case, the lognormal type and Rayleigh distribution function are used for data fitting. After comparing the χ-square error and the determination coefficient of fitting, we find that the Rayleigh distribution function (shown by the dashed curve in Figure 3) is more suitable for the grain growth behavior description of U_3Si_2 during the thermal treatment.

4 Conclusion

In our work, a phase-field simulation was provided at a temperature of 600 K at grids with characteristic length $L = N\Delta l$ with $N = 256$ and 512 by using the implicit Fourier transformation method. Grains' morphology evolution shows grain nucleation and growth simultaneously, and the larger ones coarsen by consuming smaller ones, leading to a decrease in the grain number at the latter stage. The grain area increases in time, according to the linear time law, while the mean grain radius increases in time in a power law form $a(t) \propto t^z$ with the scaling growth exponent z = 0.42, which is quite close to the theoretically predicted value 1/2. Finally, the grain size distribution of U_3Si_2 obeys the Rayleigh function by comparing the χ-square error and determination coefficient with a lognormal type fitting. Our results investigate grain growth dynamics and provide a quantitative description of grain size distribution in U_3Si_2 under the ideal circumstance, which not only lays a solid foundation for grain morphology investigation with voids and other second-phase precipitates but also is helpful for the study of grain subdivision, amorphization, and swelling in U_3Si_2.

Data availability statement

The original contributions presented in the study are included in the article/supplementary material; further inquiries can be directed to the corresponding authors.

Author contributions

CM: model development, data analysis, and writing the original draft. MZ: data analysis, checking, and writing the original draft. TX: conceptualization and methodology. LW: conceptualization, supervision, and funding acquisition. RP: methodology and data analysis. JQ: software, methodology, and data analysis. JZ: methodology, software, and supervision.

Funding

This work is supported by the Sichuan Science and Technology Program (Grant no. 2022JDGD0040).

Conflict of interest

The authors declare that the research was conducted in the absence of any commercial or financial relationships that could be construed as a potential conflict of interest.

Publisher's note

References

Aagesen, L. K., Andersson, D., Beller, B. W., Cooper, M. W., Gamble, K. A., Miao, Y., et al. (2020). Phase-field simulations of intergranular fission gas bubble behavior in U_3Si_2 nuclear fuel. *J. Nucl. Mater.* 541, 152415. doi:10.1016/j.jnucmat.2020.152415

Ahmed, K., Pakarinen, J., Allen, T., and El-Azab, A. (2014). Phase field simulation of grain growth in porous uranium dioxide. *J. Nucl. Mater.* 446, 90–99. doi:10.1016/j.jnucmat.2013.11.036

Ansari, T. Q., Huang, H., and Shi, S. Q. (2021). Phase field modeling for the morphological and microstructural evolution of metallic materials under environmental attack. *npj Comput. Mat.* 7 (1), 143–221. doi:10.1038/s41524-021-00612-7

Atkinson Hv, H. V. (1988). Overview no 65: Theories of normal grain growth in pure singlephase systems. *Acta Metall.* 36, 469.

Azeem, M. M., Wang, Q., Zhang, Y., Liu, S., and Zubair, M. (2019). Effect of grain boundary on diffusion of P in alpha-Fe: A molecular dynamics study. *Front. Phys.* 7, 97. doi:10.3389/fphy.2019.00097

Beeler, B., Baskes, M., Andersson, D., Cooper, M. W., and Zhang, Y. (2019). Molecular dynamics investigation of grain boundaries and surfaces in U_3Si_2. *J. Nucl. Mater.* 514, 290–298. doi:10.1016/j.jnucmat.2018.12.008

Bischoff, J., Blanpain, P., Brachet, J. C., Lorrette, C., Ambard, A., Strumpell, J., et al. (2016). *Development of fuels with enhanced accident tolerance, accident tolerant fuel concepts for light water reactors*. United States of America: IAEA Tecdoc. 1797:22-29.

Blikstein, P., and Tschiptschin, A. P. (1999). Monte Carlo simulation of grain growth. *Mat. Res.* 2, 133–137. doi:10.1590/s1516-14391999000300004

Chen, L. Q. (2002). Phase-field models for microstructure evolution. *Annu. Rev. Mat. Res.* 32, 113–140. doi:10.1146/annurev.matsci.32.112001.132041

Chen, L. Q., and Yang, W. (1994). Computer simulation of the domain dynamics of a quenched system with a large number of nonconserved order parameters: The grain-growth kinetics. *Phys. Rev. B* 50, 15752–15756. doi:10.1103/physrevb.50.15752

Cheniour, A., Tonks, M., Gong, B., Yao, T., He, L., Harp, J. M., et al. (2020). Development of a grain growth model for U_3Si_2 using experimental data, phase field simulation and molecular dynamics. *J. Nucl. Mater.* 532, 152069. doi:10.1016/j.jnucmat.2020.152069

Davidge, R. W., and Evans, A. G. (1969). The strength and fracture of stoichiometricpolycrystalline UO_2. *J. Nucl. Mater.* 33, 249–260. doi:10.1016/0022-3115(69)90019-1

Fan, D., and Chen, L. Q. (1997). Computer simulation of grain growth using a continuum field model. *Acta Mat.* 45, 611–622. doi:10.1016/s1359-6454(96)00200-5

Forsberg, K., and Massih, A. R. (2001). "Theory of fission gas release during grain growth," in the 16th International Conference on Structural Mechanics in Reactor Technology, Washington DC, August 2001.

Frost, H. J., and Thopson, C. V. (1996). Computer simulation of grain growth. *Curr. Opin. Solid State Mat. Sci.* 1, 361–368. doi:10.1016/s1359-0286(96)80026-x

Harding, J. H., and Martin, D. G. (1989). A recommendation for the thermal conductivity of UO_2. *J. Nucl. Mater.* 166 (3), 223–226. doi:10.1016/0022-3115(89)90218-3

III Krill, C. E., and Chen, L. Q. (2002). Computer simulation of 3D grain growth using a phase-field model. *Acta Mat.* 50, 3059–3075. doi:10.1016/s1359-6454(02)00084-8

Kapoor, K., Ahmad, A., Laksminarayana, A., and Hemanth Rao, G. V. (2007). Fracture properties of sintered UO_2 ceramic pellets with duplex microstructure. *J. Nucl. Mater.* 366, 87–98. doi:10.1016/j.jnucmat.2006.12.044

Kobayashi, R., Warren, J. A., and Carter, W. C. (2000). A continuum model of grain boundaries. *Phys. D. Nonlinear Phenom.* 140, 141–150. doi:10.1016/s0167-2789(00)00023-3

Li, Y., Hu, S., Sun, X., and Stan, M. (2017). A review: Applications of the phase field method in predicting microstructure and property evolution of irradiated nuclear materials. *npj Comput. Mat.* 3, 16. doi:10.1038/s41524-017-0018-y

Li, Y., Zhou, J., Li, R., and Zhang, Q. (2021). Molecular dynamics simulation of zener pinning by differently shaped and oriented particles. *Front. Mat.* 8, 152. doi:10.3389/fmats.2021.682422

Liang, L., Mei, Z. G., Kim, Y. S., Ye, B., Hofman, G., Anitescu, M., et al. (2016). Mesoscale model for fission-induced recrystallization in U-7Mo alloy. *Comput. Mat. Sci.* 124, 228–237. doi:10.1016/j.commatsci.2016.07.033

Liu, Y., Baudin, T., and Penelle, R. (1997). Simulation of normal grain growth by cellular automata. *Scr. Mat.* 34, 1679–1683. doi:10.1016/1359-6462(96)00055-3

Lobkovsky, A. E., and Warren, J. A. (2001). Sharp interface limit of a phase-field model of crystal grains. *Phys. Rev. E* 63, 051605. doi:10.1103/physreve.63.051605

Mei, Z. G., Liang, L., Kim, Y. S., Wiencek, T., O'Hare, E., Yacout, A. M., et al. (2016). Grain growth in U-7Mo alloy: A combined first-principles and phase field study. *J. Nucl. Mater.* 473, 300–308. doi:10.1016/j.jnucmat.2016.01.027

Miao, Y. B., Gamble, K. A., Andersson, D., Mei, Z. G., and Yacout, A. M. (2018). Rate theory scenarios study on fission gas behavior of U_3Si_2 under LOCA conditions in LWRs. *Nucl. Eng. Des.* 326, 371–382. doi:10.1016/j.nucengdes.2017.11.034

Miao, Y. B., Gamble, K. A., Andersson, D., Ye, B., Mei, Z. G., Hofman, G., et al. (2017). Gaseous swelling of U_3Si_2 during steady-state LWR operation: A rate theory investigation. *Nucl. Eng. Des.* 322, 336–344. doi:10.1016/j.nucengdes.2017.07.008

Millett, P. C., Wolf, D., Desai, T., Rokkam, S., and El-Azab, A. (2008). Phase-field simulation of thermal conductivity in porous polycrystalline microstructures. *J. Appl. Phys.* 104, 033512. doi:10.1063/1.2964116

Moelans, N., Blanpain, B., and Wollants, P. (2008). An introduction to phase field modeling of microstructure evolution. *Calphad* 32, 268–294. doi:10.1016/j.calphad.2007.11.003

Moelans, N., Blanpain, B., and Wollants, P. (2008). Quantitative analysis of grain boundary properties in a generalized phase field model for grain growth in anisotropic systems. *Phys. Rev. B* 78, 024113. doi:10.1103/physrevb.78.024113

Oguma, M. (1982). Microstructure effects on fracture strength of UO_2 fuel pellets. *J. Nucl. Sci. Technol.* 19, 1005–1014. doi:10.1080/18811248.1982.9734249

Rest, J., and Hofman, G. L. (2004). A model for fission-gas-bubble behavior in amorphous uranium silicide compounds. *J. Nucl. Mater.* 325, 107–117. doi:10.1016/j.jnucmat.2003.11.008

Srezende, J. L. L., Pezzolla, F., Nestler, B., SeeBelberg, M., Prieler, R., Schmitz, G., et al. (1996). A phasefield concept for multiphase systems. *Phys. D. Nonlinear Phenom.* 94, 135–147. doi:10.1016/0167-2789(95)00298-7

Terrani, K. A., Wang, D., Ott, L. J., and Montgomery, R. O. (2014). The effect of fuel thermal conductivity on the behavior of LWR cores during loss-of-coolant accidents. *J. Nucl. Mater.* 448 (1-3), 512–519. doi:10.1016/j.jnucmat.2013.09.051

Tonks, M. R., Zhang, Y., Bai, X., and Millett, P. C. (2014). Demonstrating the temperature gradient impact on grain growth in UO_2 using the phase field method. *Mat. Res. Lett.* 2, 23–28. doi:10.1080/21663831.2013.849300

Vaz, M. F., and Fortes, M. A. (1988). Grain size distribution: The lognormal and the gamma distribution functions. *Scr. Metall.* 22 (1), 35–40. doi:10.1016/s0036-9748(88)80302-8

Wakai, F., Enomoto, N., and Ogawa, H. (2000). Three dimensional microstructural evolution in ideal grain growth general statistics. *Acta Mat.* 48, 1297–1311. doi:10.1016/s1359-6454(99)00405-x

Wen, Y. H., Wang, B., Simmons, J. P., and Wang, Y. (2006). A phase-field model for heat treatment applications in Ni-based alloys. *Acta mater.* 54 (8), 2087–2099. doi:10.1016/j.actamat.2006.01.001

Westinghouse Electric Company (2015). *Development of LWR fuels with enhanced accident tolerance*. United States: Final Technical Report.

Weygand, D., Brechet, Y., and Lepinoux, A. (1998). A vertex dynamics simulation of grain growth in two dimensions. *Philos. Mag. B* 78, 329–352. doi:10.1080/014186398258014

White, J. T., Nelson, A. T., Dunwoody, J. T., Byler, D., Safarik, D., and McClellan, K. (2015). Thermophysical properties of U_3Si_2 to 1773 K. *J. Nucl. Mater.* 464, 275–280. doi:10.1016/j.jnucmat.2015.04.031

Zhou, W., and Zhou, W. (2018). Enhanced thermal conductivity accident tolerant fuels for improved reactor safety–A comprehensive review. *Ann. Nucl. Energy* 119, 66–86. doi:10.1016/j.anucene.2018.04.040